Journal of Magnetism and Magnetic Materials 641 (2026) 173817

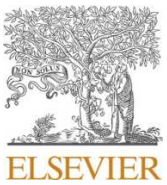

Contents lists available at ScienceDirect

Journal of Magnetism and Magnetic Materials

journal homepage: www.elsevier.com/locate/jmmm

A novel broken wire localization method for bridge cables based on multi-component magnetic flux leakage testing

Huanze Liu [a], Lingsi Sun [a], Runyu Wang [a], Yiqing Zou [b], Xinjun Wu [a,*]

[a] School of Mechanical Science & Engineering, Huazhong University of Science and Technology, Wuhan 430074, China
[b] Liuzhou OVM Machinery Co., Ltd., Liuzhou 545000, China

ARTICLE INFO

Keywords:
Bridge cables
Multi-component MFL signals
Broken wire
Magnetic dipole model
Defect localization

ABSTRACT

Bridge cables, as one of the critical load-bearing elements in cable-stayed bridges, are prone to hidden internal defects that are difficult to detect. In conventional magnetic flux leakage (MFL) testing, the magnetic field decays rapidly with depth, which hinders defect localization. To overcome this limitation, this study proposes a defect localization method based on multi-component MFL signals. Based on the magnetic dipole model (MDM) of a single broken wire, the spatial-domain summation preprocessing in the circumferential direction is proposed to enhance weak responses. For axial localization, cross-validation of the summed differential axial component and the radial component improves robustness. In addition, an asymmetric peak–valley full width at half-maximum (APV-FWHM) feature is introduced for depth localization, which reduces amplitude dependence and decouples depth localization from circumferential positioning. In order to validate the method, an experimental platform for bridge cable based on MFL testing was established. Experimental validation on a PECS7–127 cable successfully detected all broken-wire defects at depths of up to 42 mm with a 95% confidence interval of 97.9–100%. The axial localization results from different components indicated strong consistency, reaching 94.9% accuracy within a ± 5 mm tolerance. In addition, circumferential defect regions were effectively identified, and radial localization achieved 97.7% accuracy when a tolerance of ±1 layer was permitted. These findings provide preliminary validation of the feasibility and reliability of the proposed method for testing and localizing a single broken wire defect in bridge cables using multi-component MFL signals.

1. Introduction

Bridge cables, serving as one of the critical load-bearing elements in cable-stayed bridges, suspension bridges, and tied-arch bridges, are subjected during service to the coupled effects of traffic loads, wind loads, and aggressive environmental conditions [1,2]. Under such circumstances, defects such as corrosion and broken wires could occur inside the cable, while their hidden nature renders conventional visual detection ineffective for timely identification. If such defects continue to propagate, the service life may be significantly shortened [3], and in severe cases, its safe operation could be compromised.

Magnetic flux leakage (MFL) testing, as a widely adopted non-destructive testing (NDT) technique, has been extensively applied in steel wire ropes, pipelines, and rails [4]. Given its suitability for detecting internal defects in ferromagnetic materials and its proven practicality and deployability in engineering applications, MFL is also well suited for the testing of bridge cables.

Bridge cables, however, differ markedly from conventional wire ropes. They exhibit larger diameters and are covered by a polyethylene (PE) sheath that introduces significant lift-off distance. The lift-off distance leads to significant attenuation and spatial smoothing of the external magnetic field. As a result, the acquired signal is dominated by its axial component, and it was traditionally assumed that the radial and circumferential components carry little value for identifying defects [5,6]. As a representative of this view, Christen investigated cross-sectional localization of defects in stay cables by modeling each defect as an equivalent magnetic dipole and fitting this analytical expression to the axial pickup coil signals acquired on the cable surface [5]. This approach represented an exploratory attempt to infer defect positions from single-component data. Subsequently, Ben employed a three-dimensional finite element model of a broken-wire defect and revealed the distribution of the axial and circumferential components, without experimental validation [7]. These results suggest that, even under significant lift-off distance and predominantly axial

* Corresponding author.
E-mail address: xinjunwu@hust.edu.cn (X. Wu).

https://doi.org/10.1016/j.jmmm.2026.173817
Received 22 October 2025; Received in revised form 23 December 2025; Accepted 6 January 2026
Available online 9 January 2026

magnetization, radial and circumferential components may still retain discriminative information.

Despite these indications, current practical testing for bridge cables mainly provides preliminary axial defect location rather than triaxial localization [8]. In particular, identifying the circumferential position of a defect and determining whether it is located near the surface or in a deeper layer remain challenging [9]. Such localization information is essential for targeted repair and window-opening verification during maintenance, and serves as the link between defect detection and subsequent safety assessment [10].

Achieving reliable three-dimensional localization of defects generally requires sufficient and complementary information from multi-component signals, rather than relying on a single dominant component. This requirement can be addressed in two ways. One is enriching vector information through multi-component acquisition, another is enriching spatial information through multi-channel sampling. Subsequently, signal processing is applied to extract localization information in the axial, circumferential, and depth directions.

From the perspective of multi-component acquisition, multi-component sensing has gained increasing application in recent years [11–13]. For small-diameter wire ropes, Chen employed a 30-channel array to acquire axial, radial, and circumferential MFL signals, indicating that multi-component fields provide complementary information that improves the detectability for broken wires [14]. For pipelines, Chen proposed a cascaded detection and sizing framework, in which triaxial MFL samples collected by a 240-channel detection robot were integrated with deep learning and physics-informed models, yielding substantial gains in defect identification and sizing accuracy [15]. In the railway field, Gong conducted vehicle-borne multi-component MFL testing with triaxial Hall-sensor arrays and reported that varying array configurations extract richer feature descriptors of rail-head cracks [16]. The above studies indicate that multi-component acquisition is an effective means of increasing information diversity for defect characterization and localization. However, in the specific domain of bridge cable testing, such multi-component experimental research remains unexplored.

From the perspective of multi-channel sampling, multi-channel sampling enhances spatial coverage and redundancy, which is particularly beneficial for weak defect responses. On the practical side, Sun developed a circumferential multi-channel detection system employing a simulated uniaxial Hall-sensor array with multiplexing techniques [8,17]. This configuration expanded information coverage, underscoring the need for multi-channel acquisition and multi-component analysis to improve defect separability in bridge cables. Evidence from other MFL domains further supports the effectiveness of multi-channel acquisition and analysis for enhancing defect separability. Xue investigated wire ropes with a circumferential inductive coil array and using an adaptive pipeline of differencing, empirical mode decomposition (EMD), wavelet denoising, and correlation-guided fusion, achieved a significantly higher signal-to-noise ratio (SNR) than single-channel signals [18]. Liu proposed a scheme for pipelines in which multi-channel Hall signals were fused within a three-dimensional dipole-inversion framework, yielding more efficient depth quantification and reducing estimation errors to below 10% [19]. These studies point to a consistent trend that multi-channel sampling can provide a practical information basis under weak response conditions.

In summary, these studies indicate that multi-component and multi-channel MFL testing can improve the detectability of weak defects. Nevertheless, the effective use of triaxial information for practical triaxial localization in bridge cable testing remains insufficiently validated. This issue still requires a validated, physically interpretable signal-processing workflow tailored to bridge cable testing. To establish a controlled basis, this study begins with a single broken-wire defect under a controlled lift-off condition. A single broken wire provides a more stringent detectability test, as its response amplitude is lower than that of multiple-break cases.

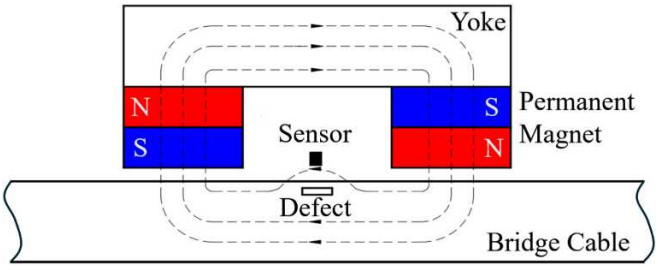

Fig. 1. Principle of MFL testing for bridge cables.

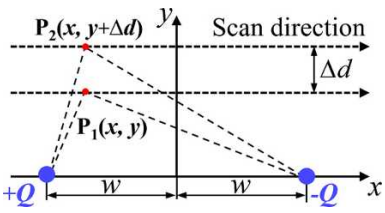

Fig. 2. MDM of a single broken-wire defect in a bridge cable.

Based on the above analysis, this study proposes a defect-localization method for bridge cables based on multi-component MFL signals. First, circumferential spatial-domain summation is performed on differential components to improve SNR of deep defects. Second, a workflow of the method is then developed. The axial position is cross-validated by the summed differential axial signal and radial signal, the circumferential region is identified from the peak of the differential axial component, and the defect depth is estimated using an asymmetric peak–valley full width at half-maximum (APV-FWHM) feature that reduces amplitude dependence and decouples depth estimation from circumferential positioning. Finally, an experimental platform was established and applied to a bridge cable specimen to validate the proposed method. The remainder of the paper is organized as follows: Section 2 introduces the magnetic dipole model (MDM) and the multi-component localization workflow; Section 3 describes the experimental setup and specimen; Section 4 presents the experimental results and discussion; and Section 5 concludes the paper and outlines future work.

2. Method

2.1. MDM of a single broken wire

The principle of MFL testing for bridge cables is shown in Fig. 1. A permanent magnet is employed to magnetize the cable. When a defect is present inside the cable, local permeability decreases and magnetic reluctance increases, causing a portion of the magnetic flux to leak from the steel into the surrounding air. In the absence of an internal defect, the magnetic flux primarily closes along the cable path and returns through the yoke. By placing magnetic sensors on the cable surface, the leakage field induced by defects can be acquired. The amplitude, waveform, and spatial distribution of the signals provide information for determining the location of the defect.

Considering a single broken-wire defect located within the bridge cable, all steel wires are assumed to be magnetically saturated by the permanent magnet during the MFL testing process [20,21]. In the model, inter-wire interactions are neglected, and the leakage field generated by the broken wire is assumed not to be significantly altered by the surrounding intact wires. Reference [4] reported that in the two-dimensional case, a broken wire with a width of $2w$ can be modeled by assuming magnetic charges of $\pm Q$ on both sides of the defect, as shown in Fig. 2. One positive charge $+Q$ is located at $x = -w$, and another negative charge $-Q$ is located at $x = +w$.

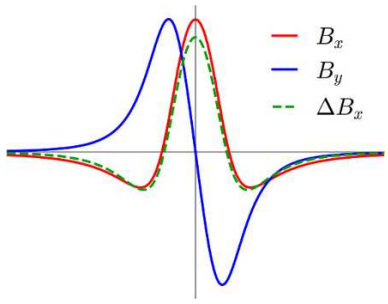

Fig. 3. Normalized typical MFL signal shapes of a single broken wire.

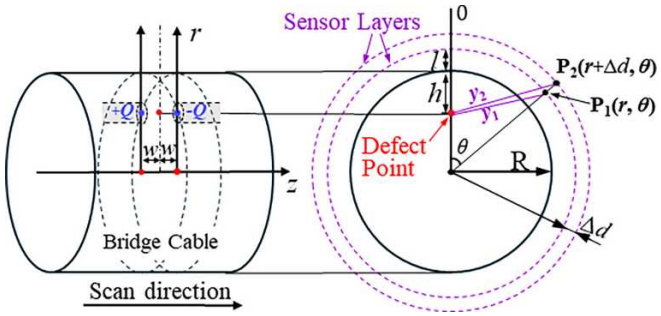

Fig. 4. MDM for a single broken-wire defect in bridge cable.

The leakage magnetic field produced by a magnetic dipole pair is expressed in components at an in-plane point (x, y) (as)

$$B_x(x,y,w,Q) = \frac{\mu_0 Q}{4\pi}\left(\frac{x+w}{\left((x+w)^2+y^2\right)^{3/2}} - \frac{x-w}{\left((x-w)^2+y^2\right)^{3/2}}\right) \quad (1)$$

$$B_y(x,y,w,Q) = \frac{\mu_0 Q}{4\pi}\left(\frac{y}{\left((x+w)^2+y^2\right)^{3/2}} - \frac{y}{\left((x-w)^2+y^2\right)^{3/2}}\right) \quad (2)$$

In related studies, the inter-layer differential sensors were employed to acquire the MFL signals [22,23]. This configuration enhances the leakage field response by differentiating signals from two vertically offset positions, expressed as:

$$\Delta B_x(x,y,w,Q,\Delta d) = B_x(x,y,w,Q) - B_x(x,y+\Delta d,w,Q) \quad (3)$$

To facilitate comparison of waveform characteristics, the normalized typical MFL signals of a single broken wire are shown in Fig. 3 along the scan direction. Both B_x and ΔB_x reach their peak values at the defect center, whereas B_y becomes zero at this position, showing an antisymmetric distribution on both sides of the defect.

2.2. Multi-component signals of MFL testing

A cylindrical coordinate system (r, θ, z) is defined on the bridge cable, as shown in Fig. 4. The sensors are circumferentially arranged, and the z-axis corresponds to the scan direction discussed in Section 2.1.

The parameter w corresponds to half of the broken-wire defect width, with the defect center defined at $z = 0$. On the cross-sectional projection plane, y is defined as the projection of the sensor–defect line, consistent with the definition of y in Section 2.1. The parameter R is the radius of the outer circumscribed circle of the parallel wires and is treated as a constant. The lift-off distance l includes the PE sheath thickness and the sensor–sheath gap. For a single scan, l can be assumed constant. The variable h represents the depth direction from the cable surface toward its center, and Δd denotes the distance between sensor layers.

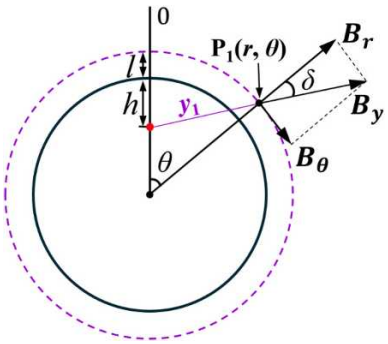

Fig. 5. Cross-sectional projection plane.

For a circumferential angle θ with $-\pi \le \theta \le \pi$, the resulting distances y_1 and y_2 are given by eqs. (4) and (5), respectively.

$$y_1 = \sqrt{(R-h)^2 + (R+l)^2 - 2(R-h)(R+l)\cos\theta} \quad (4)$$

$$y_2 = \sqrt{(R-h)^2 + (R+l+\Delta d)^2 - 2(R-h)(R+l+\Delta d)\cos\theta} \quad (5)$$

The axial component of the magnetic field on the cross section, aligned with the scan direction, is modeled as:

$$B_z(z,y;w,Q) = \frac{\mu_0 Q}{4\pi}\left(\frac{z+w}{\left((z+w)^2+y^2\right)^{3/2}} - \frac{z-w}{\left((z-w)^2+y^2\right)^{3/2}}\right) \quad (6)$$

The radial inter-layer differential signal is defined by differentiating B_z at y_1 and y_2:

$$\Delta B_z(\theta,z;R,h,l,\Delta d,w,Q) = B_z(z,y_1;w,Q) - B_z(z,y_2;w,Q) \quad (7)$$

In the cross-sectional projection plane as shown in Fig. 5, the angle δ is defined as the angle between the sensor–defect line and the radial direction r. The magnetic flux density components B_r and B_θ represent the radial and circumferential directions respectively, where B_θ is orthogonal to B_r.

The component B_y is given by:

$$B_y(\theta,z;R,h,l,w,Q) = \frac{\mu_0 Q}{4\pi}\left[\frac{y_1}{\left((z+w)^2+y_1^2\right)^{3/2}} - \frac{y_1}{\left((z-w)^2+y_1^2\right)^{3/2}}\right] \quad (8)$$

The circumferential and radial components are then obtained by:

$$B_\theta(\theta,z;R,h,l,w,Q) = \sin\delta \bullet B_y(\theta,z;R,h,l,w,Q) \quad (9)$$

$$B_r(\theta,z;R,h,l,w,Q) = \cos\delta \bullet B_y(\theta,z;R,h,l,w,Q) \quad (10)$$

The geometric relationships for δ are defined as:

$$\sin\delta = \frac{(R-h)\sin\theta}{y_1} \quad (11)$$

$$\cos\delta = \frac{(R+l)^2 + y_1^2 - (R-h)^2}{2(R+l)y_1} \quad (12)$$

In the practical MFL testing, the acquired signal $B_{acquire}$ detected by the sensor can be expressed as:

$$B_{acquire} = B_{background} + B_{wire} \quad (13)$$

where $B_{background}$ denotes the background field generated by the magnetizer, and B_{wire} represents the magnetic field induced by the defect.

Along the axial direction, differential processing between two sensor positions effectively suppresses the background field [8], so that the

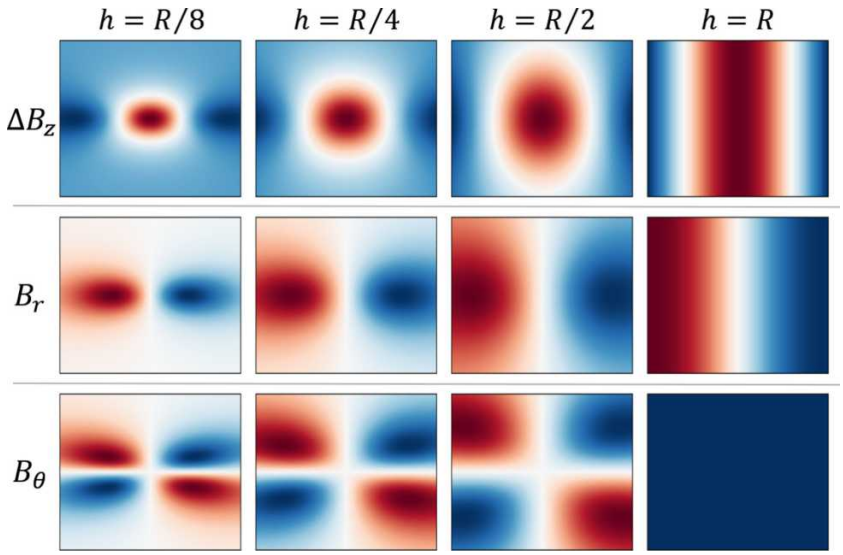

Fig. 6. Typical signals from a single broken wire at different depths in the bridge cable.

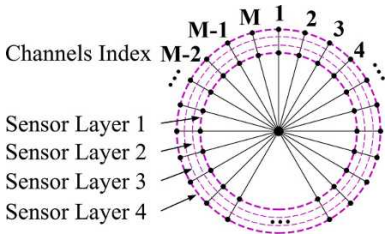

Fig. 7. Probe array with a finite number of M circumferential channels.

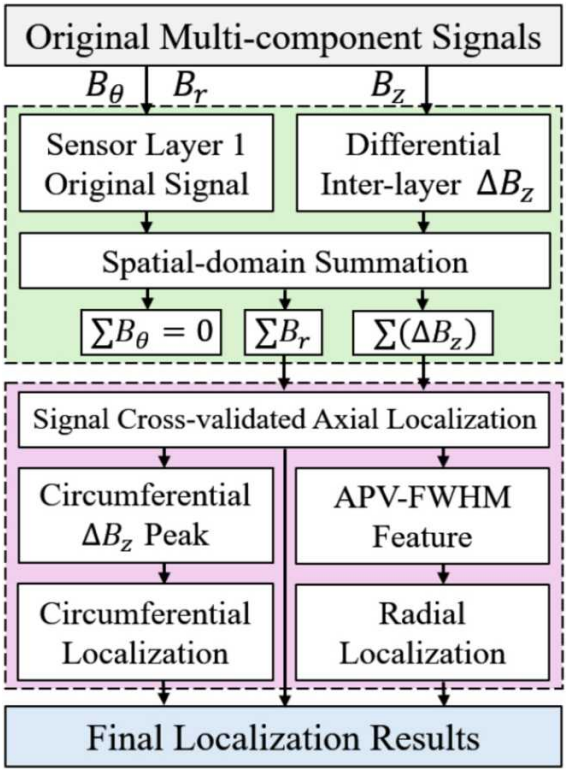

Fig. 8. Flowchart of the proposed broken wire localization method.

acquired differential signal can be approximated as the differential component of $B_{wire,z}$:

$$\Delta B_{acq,z} \approx \Delta B_{wire,z} \tag{14}$$

In theory, the background magnetization field in the circumferential and radial components of the MFL signals is much smaller and can be neglected. These responses are most pronounced in the innermost sensor layer, which is selected for subsequent analysis. These signals can be approximated by the corresponding component as:

$$B_{acq,r} \approx B_{wire,r} \tag{15}$$

$$B_{acq,\theta} \approx B_{wire,\theta} \tag{16}$$

All subsequent analyses in this study are based on the above approximations. As shown in Fig. 6, the typical signals of a single broken wire in the bridge cable indicate distinct characteristics at different depths. The columns represent increasing depth from left to right, and the rows correspond to ΔB_z, B_r and B_θ.

2.3. Broken wire localization method

In the practical testing, the sensor array consists of a finite number M of circumferential channels, as shown in Fig. 7. These channels provide a spatial sampling of the circumferential MFL signals.

The workflow of the proposed broken wire localization method is summarized in Fig. 8. It shows the preprocessing of multi-component signals through circumferential spatial-domain summation, followed by axial, circumferential, and radial localization methods.

2.3.1. Circumferential spatial-domain summation preprocessing

Given that the sensors are circumferentially arranged on the same cross section, the observation of the n-th channel at position z can be expressed as:

$$x_n(z) = s_n(z) + \eta_n(z) \tag{17}$$

where $s_n(z)$ is the axial response induced by the defect, and $\eta_n(z)$ is zero-mean noise that is independent across channels with approximately equal variance.

Since the signal adds coherently while the noise adds incoherently across independent channels, the output SNR can be expressed as:

$$\mathrm{SNR}_{\mathrm{sum}} = \mathrm{M}\cdot\mathrm{SNR}_{\mathrm{single}} \tag{18}$$

In decibels, this relationship can be written as:

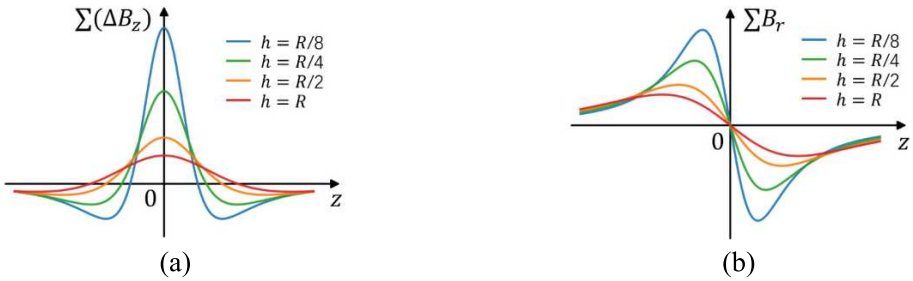

Fig. 9. Typical circumferentially summed MFL signals of a single broken-wire defect at different depth: (a) Summation of differential axial component; (b) Summation of radial component.

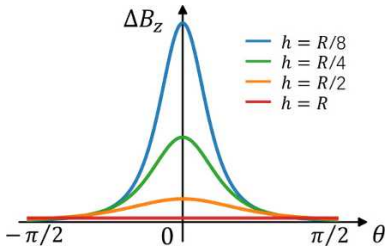

Fig. 10. Circumferential localization of defect analyzed using ΔB_z signal at different depth.

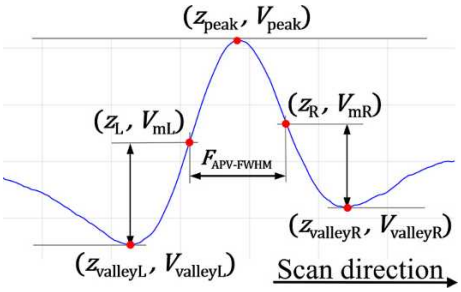

Fig. 11. Representation of the APV-FWHM.

$$SNR_{dB,sum} = SNR_{dB,single} + 10\log_{10}M \quad (19)$$

Therefore, circumferential summation in the spatial domain enhances the SNR of deep-defect responses by $10\log_{10}M$ dB. When the defect is offset from the cable center, the number of effectively contributing channels decreases. Nevertheless, the SNR of summed signals remains markedly higher than that of a single channel as long as a subset of channels contribute effectively.

2.3.2. Signal cross-validation for axial localization

To enhance the reliability of defect testing, the signal cross-validation for axial localization is employed. As shown in Fig. 9 (a), the curves correspond to different defect depths ($0 \le h \le R$). The circumferential summation of ΔB_z reaches its peak at the defect location for all depths, providing a reliable indicator for axial localization. For deeper defects, the amplitude of the summed signal is more pronounced than the single-channel response due to the contribution of circumferential summation. Similarly, Fig. 9 (b) shows that the circumferential summation of B_r always crosses zero at the defect location for different defect depths ($0 \le h \le R$). In practice, the defect position can be accurately determined by identifying the midpoint between the adjacent peak and valley of the summed radial response, thereby enabling signal cross-validation of the axial location. Meanwhile, the summation of B_θ indicated a centrosymmetric feature along the circumferential direction and remained consistently zero.

2.3.3. Circumferential localization

On the circular cross section at the defect center, the defect was located by analyzing the differential axial component. As shown in Fig. 10, the curves correspond to different defect depths ($0 \le h \le R$). The ΔB_z signal reached its maximum at the defect location, providing a reliable basis for circumferential localization. In addition, the signal amplitude decreases symmetrically on both sides of the peak, reflecting the local response induced by the broken wire. The sharpness and magnitude of the peak depend on defect depth.

2.3.4. Radial localization

Assuming a fixed width w, the depth localization in reference [8] relied on the amplitude directly above the defect at the sensor of interest, so that circumferential localization had to be achieved first because the defect location is generally unknown prior to testing. In other words, the radial and circumferential localization criteria are coupled. In Section 2.3.2, the spatial distribution of the MFL signals shows that increasing defect depth causes the axial profile of the broken-wire response to become progressively broader. To quantify this depth-related broadening, this study extends the classical full width at half maximum (FWHM) concept to the asymmetric peak–valley waveform and adopts the asymmetric peak–valley full width at half-maximum (APV-FWHM) as the depth feature [24]. APV-FWHM is defined as the axial distance between the midpoints of the left and right peak–valley pairs, as shown in Fig. 11.

Along the scan direction, the peak of the defect response is denoted as (z_{peak}, V_{peak}), and the nearest valleys on the left and right are $(z_{valleyL}, V_{valleyL})$ and $(z_{valleyR}, V_{valleyR})$, respectively. The corresponding midpoints of the left and right peak–valley pairs are then given by eqs. (20) and (21):

$$V_{mL} = \frac{1}{2}V_{peak} + \frac{1}{2}V_{valleyL} \quad (20)$$

$$V_{mR} = \frac{1}{2}V_{peak} + \frac{1}{2}V_{valleyR} \quad (21)$$

The intersections of the signal curve with these midpoint values are denoted as (z_L, V_{mL}) and (z_R, V_{mR}). The APV-FWHM can be defined as:

$$F_{APV-FWHM} = z_R - z_L \quad (22)$$

3. Experimental setup

3.1. Experimental platform

In order to validate the proposed method, an experimental platform for bridge cable based on MFL testing was established, as shown in Fig. 12. The platform mainly consists of a magnetizer, a sensor array, and a control box.

The magnetizer employs an optimized permanent-magnet configuration assembled using N52 neodymium–iron–boron (NdFeB) magnets, ensuring saturation magnetization of the steel wires in bridge cables

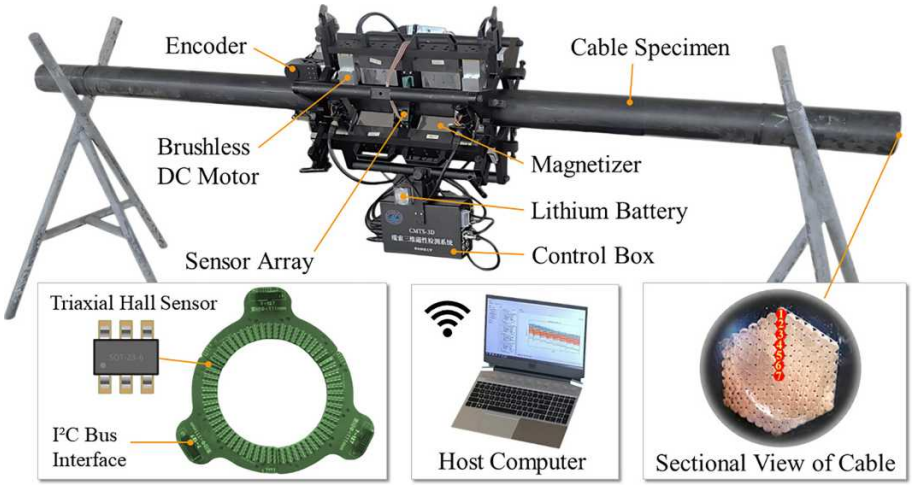

Fig. 12. Experimental platform for bridge cable using MFL testing.

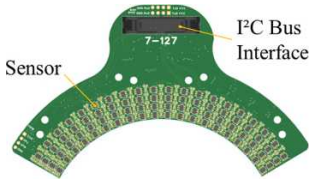

Fig. 13. Circuit board designed for a PECS7–127 cable.

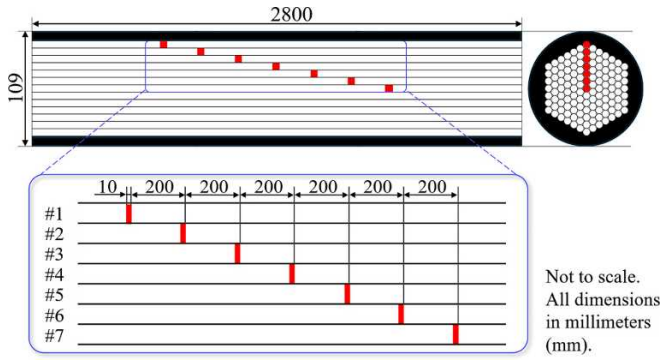

Fig. 14. Experimental cable specimen and layout of internal broken-wire defects.

during detection [25]. The sensor array is circumferentially arranged around the cable surface and divided into modular units, each equipped with Inter-Integrated Circuit (I^2C) bus interfaces. The control box is powered by a lithium battery direct current (DC) supply, while a brushless DC motor drives the magnetizer assembly along the cable specimen at a controlled scanning speed. An encoder wheel mounted on the cable surface provides displacement feedback for data sampling. All signals are collected by an acquisition module based on a field-programmable gate array (FPGA), which performs synchronous sampling and parallel data aggregation. The host computer communicates wirelessly with the controller to transmit motion commands and receive signals in real time.

In this study, the TMAG5273 triaxial digital Hall sensor (Texas Instruments) was employed. It provides a linear range of ±266 mT and an I^2C interface with runtime address reconfiguration, enabling multi-channel arrays and efficient bus management. Relative to analog Hall sensors, the digital-output architecture enables higher integration and simplifies array design and data acquisition. As shown in Fig. 13, an

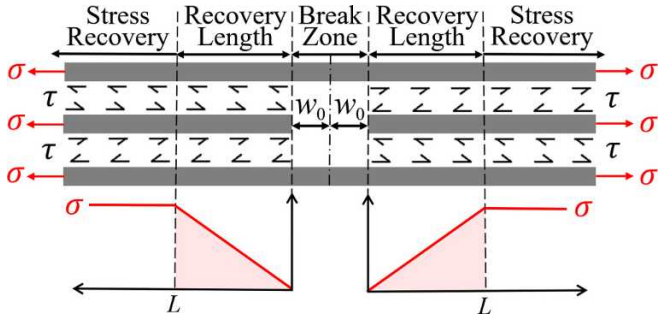

Fig. 15. Idealized stress and shear-transfer distribution of a single broken-wire defect in bridge cable.

example of a circuit board designed for a PECS7–127 cable is presented (127 steel wires of 7 mm diameter) [26]. A single circuit board had 80 triaxial Hall sensors. During testing, three circuit boards were deployed as a sensor array that surrounds the cable, providing 240 sensors arranged in four layers with an inter-layer distance of 4 mm. Within each sensor layer, 60 sensors are uniformly distributed circumferentially with an angular pitch of 6°.

3.2. Experimental cable specimen

The experimental cable specimen was 2800 mm in length, as shown in Fig. 14. It had an outer diameter of 109 mm and consisted of 127 parallel steel wires with a diameter of 7 mm [26]. Seven artificial broken-wire defects, each with a width of 10 mm, were introduced inside the specimen. All defects were placed at the same circumferential angle and were spaced 200 mm apart axially. The defect layer index was defined from #1 to #7, corresponding to the near-surface to deeper layers.

The selection of an **artificial** broken-wire width of **10 mm** has **practical engineering justification**. Bridge cables in service are typically subjected to axial tensile stress σ. When an internal steel wire fractures due to corrosion or fatigue, the released elastic strain causes **end retraction**. After **frictional load transfer** τ is re-established with adjacent wires, a single broken-wire defect in bridge cable is formed, as shown in Fig. 15.

For high-strength galvanized steel wires, the elastic modulus is $E_s \approx 200$ GPa, and the ultimate tensile strength of a 7 mm wire is $f =$ 1670 MPa − 1960 MPa [26]. Considering service stress levels of $0.45f$ − $0.55f$ [27], the applied stress range is given in (23):

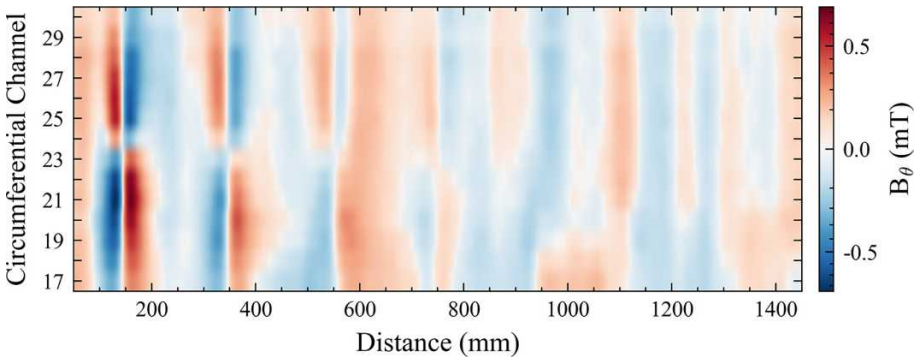

Fig. 16. Circumferential component B_θ signals for defect axial localization.

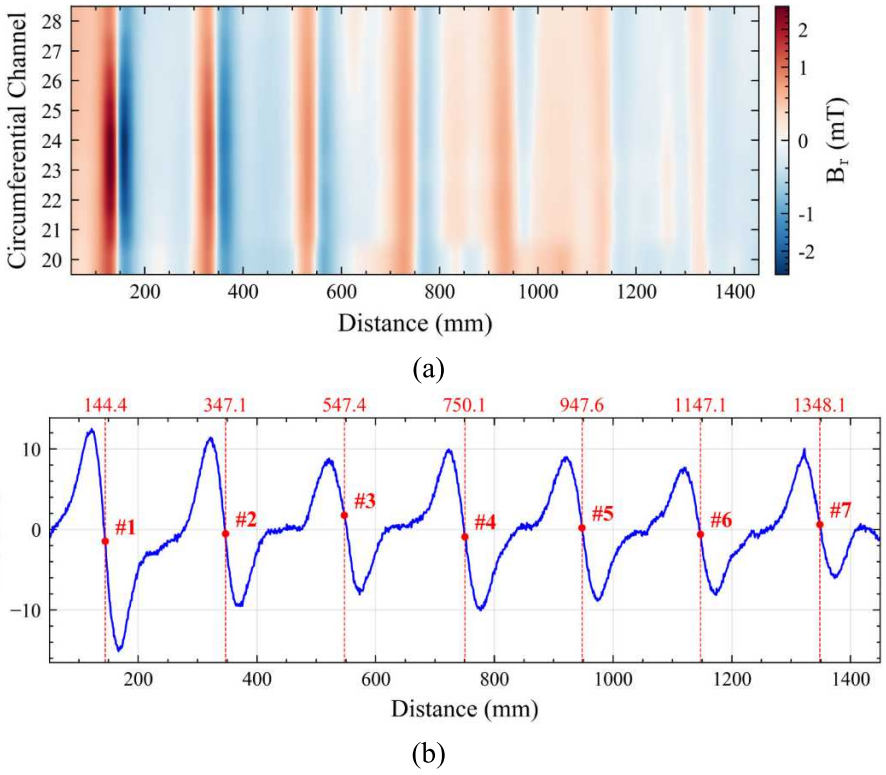

Fig. 17. Radial component signals for defect axial localization: (a) Signals B_r of the innermost sensor layer; (b) Circumferentially summed signal $\sum B_r$ of the innermost sensor layer.

$$\sigma = (0.45 - 0.55)f = 751.5\ \text{MPa} - 1078\ \text{MPa} \tag{23}$$

The corresponding strain is expressed in (24):

$$\varepsilon = \sigma / E_s = 0.38\% - 0.54\% \tag{24}$$

After fracture, the wire enters a friction-dominated transfer zone from the broken end, within which the axial force increases approximately linearly with distance until recovering to the far-field stress σ [28]. If the recovery length on one side is taken as $L_{rec} = 2\ m$ [29,30], the equivalent linear recovery length is given by (25):

$$L_{eq} = L_{rec}/2 \tag{25}$$

The single-side retraction is then (26):

$$w_0 = \varepsilon L_{eq} = 3.8\ \text{mm} - 5.4\ \text{mm} \tag{26}$$

The total width of a single broken wire, obtained by superimposing both sides, is given by (27):

$$w_{total} = 2w_0 = 7.6\ \text{mm} - 10.8\ \text{mm} \tag{27}$$

From a service-life perspective, a single-wire fracture can be regarded as an initial defect. Such a break redistributes axial force to adjacent wires, producing local stress concentration [31]. With continued service, these effects may lead to widening of the fracture zone and an increased number of broken wires. Although the long-term evolution

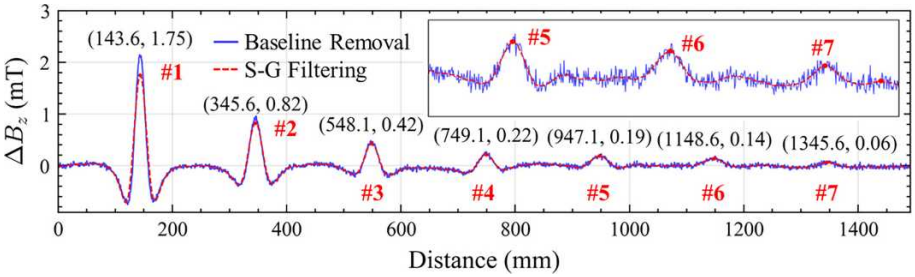

Fig. 18. Differential axial component after baseline removal and S-G filtering.

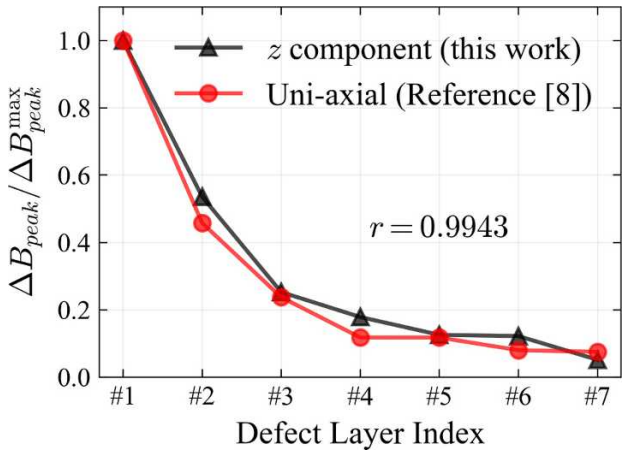

Fig. 19. Normalized comparison of differential axial component signal amplitudes.

warrants further investigation, the 10 mm artificial fracture adopted in this study provides a rational and conservative representation of the early stage of damage in bridge cables.

4. Results and discussion

Guided by the defect localization method using multi-component MFL signals in Section 2.3, the following subsections report the results of bridge-cable testing and discuss the localization performance.

4.1. Spatial-domain signal preprocessing

During the experimental testing, the sensor array scanned the cable specimen, and the multi-component signals were collected on an equally spaced grid along the scan direction with a spatial sampling resolution of 0.50 mm. One representative dataset was selected for detailed analysis. The circumferential and radial components in the innermost sensor layer were selected for subsequent analysis.

As shown in Fig. 16, the circumferential component B_θ indicated that the defect features were discernible in near-surface layers but became indistinct in the deeper layers. Therefore, the B_θ signals were not considered a primary factor in the subsequent analysis.

Fig. 17 (a) shows the radial component B_r near the defects. Multiple

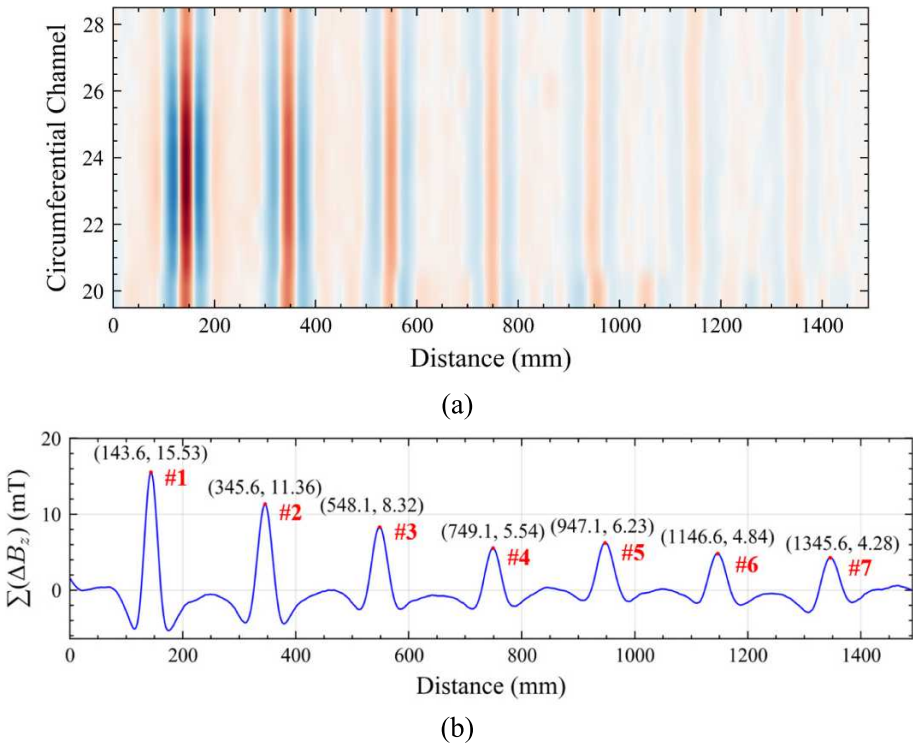

Fig. 20. Axial component differential signals for defect axial localization: (a) Differential signals ΔB_z; (b) Circumferentially summed signal $\sum(\Delta B_z)$.

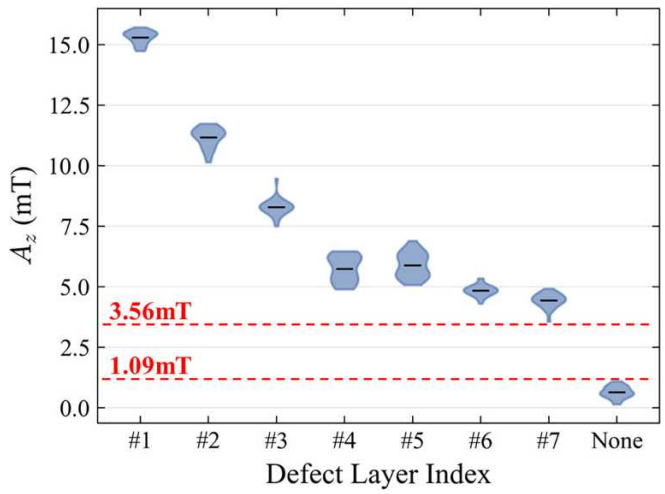

Fig. 21. Local peak amplitudes for defect and non-defect cases of Axial response A_z.

channels indicated clear responses at all seven defect positions. To improve the SNR, all signals were circumferentially summed to $\sum B_r$, as shown in Fig. 17 (b). Based on the characteristics of the signal at the defect position, the midpoint between the nearest peak and valley was taken as the defect axial position.

The differential axial component between sensor layer 1 and layer 4, referred to as the original signal, was defined by:

$$\Delta B_z^{origin} = B_{z,\text{Layer\_1}} - B_{z,\text{Layer\_4}} \tag{28}$$

To improve the quality of the original signal, a polynomial baseline fitting was first applied to remove the underlying baseline trend. This differential signal still exhibited noise spikes that impeded accurate axial localization of defects. To suppress noise while preserving signal characteristics, a Savitzky–Golay (S-G) filter with a window length of 81 and an order of 2 was applied, as shown in Fig. 18.

Seven peaks of the ΔB_z show a one-to-one correspondence with the seven defect locations. For comparison, the present results were normalized by the maximum peak value and were compared with the data reported in reference [8]. As shown in Fig. 19, the correlation coefficient $r = 0.9943$ indicated excellent agreement.

The defect peaks in the differential signals were clearly characterized, as shown in Fig. 20 (a). However, single-channel responses remained vulnerable to noise and spurious local peaks, particularly for deeper defects where the signal amplitude was weaker. To improve localization accuracy and robustness, all differential axial components were circumferentially summed, denoted as $\sum(\Delta B_z)$, to enhance the SNR of axial localization, as shown in Fig. 20 (b).

4.2. Signal cross-validation for axial localization

This section shows the signal cross-validated results for axial localization using circumferentially summed signals $\sum B_r$ and $\sum(\Delta B_z)$. The peak of $\sum(\Delta B_z)$ indicates the defect position. Because $\sum B_r$ reverses sign across the defect, the midpoint between the nearest peak and valley provides an independent axial estimate. Agreement between the two estimates confirms the position and reduces false responses from noise, drift, and vibration.

However, peak-based localization was easily confounded by spurious local maxima, which weakened separability when used alone. Accordingly, seven defects were scanned 25 times to yield 175 positive responses, while non-defect local peaks from each scan were collected as negatives. The parameter A_z was defined as the local maximum of $\sum(\Delta B_z)$, and $|A_r|$ was defined as the absolute value of local maxima and minima of $\sum B_r$. In addition, for each scan, the amplitudes of local abnormal fluctuations of A_z and $|A_r|$ in non-defect regions were extracted to form a non-defect dataset, representing the noise and environmental interference under the most unfavorable conditions.

As shown in Fig. 21, the axial response A_z exhibited a clear

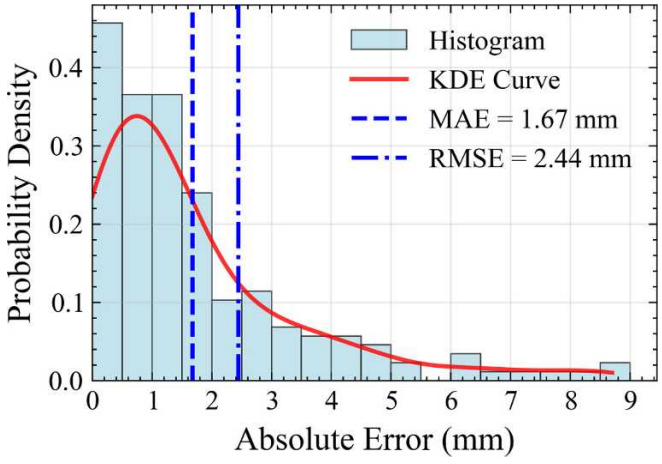

Fig. 23. Histogram of absolute errors between axial localization results from $\sum(\Delta B_z)$ and $\sum B_r$, along with KDE curve.

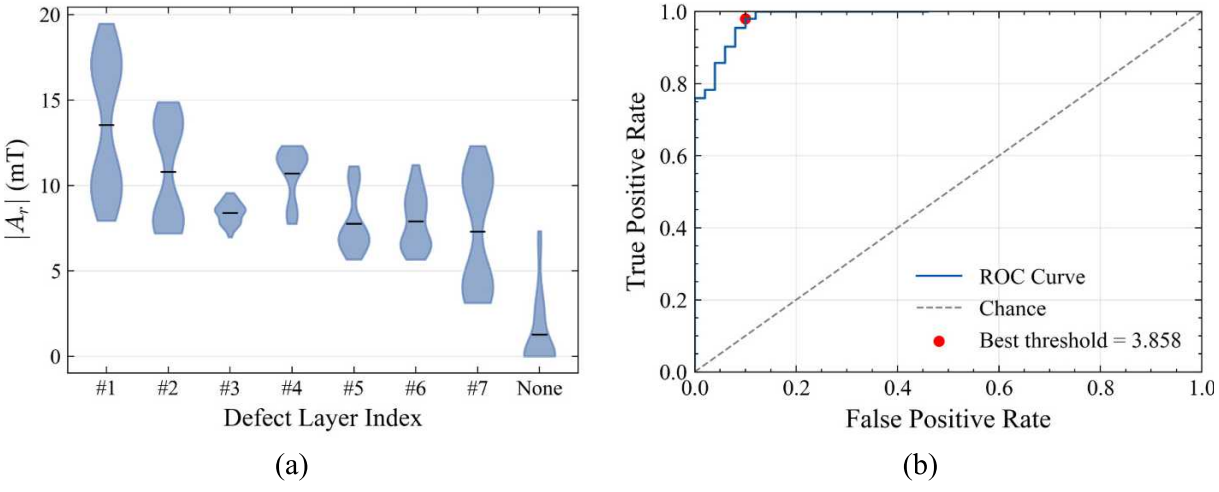

Fig. 22. Radial response $|A_r|$: (a) Local peak amplitudes for defect and non-defect cases; (b) ROC curve of local radial component $|A_r|$ (peaks)

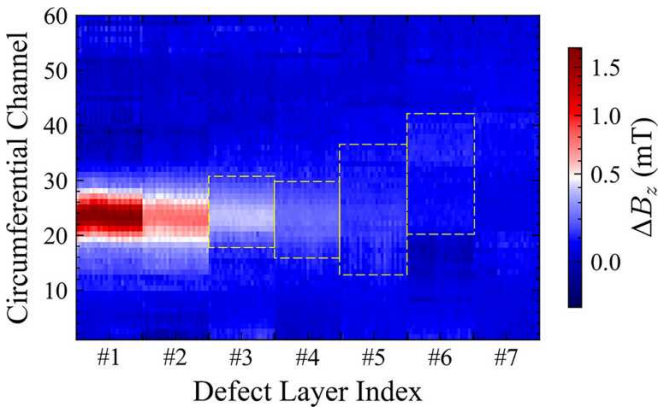

Fig. 24. Heatmaps of circumferential ΔB_z profiles at axial defect locations.

separation between defect and non-defect cases: for the deepest #7 defect, the amplitude remained above 3.56 mT, while the amplitudes of non-defect spurious peaks remained below 1.09 mT. With any threshold selected within this interval (1.09–3.56 mT), all defects in this dataset were successfully detected (175 out of 175) at depths up to 42 mm, corresponding to a 95% Clopper–Pearson confidence interval (CI) of 97.9–100%.

As shown in Fig. 22 (a), the radial response $|A_r|$ for deep defects approached the level of non-defect spurious peaks, so the threshold cannot be determined directly. Instead, the receiver-operating-characteristic (ROC) curve was used to optimize the threshold [32,33]. As shown in Fig. 22 (b), the ROC curve was constructed using defect and non-defect datasets of $|A_r|$, and the area under the curve (AUC) reached 0.985, indicating discriminative capability between defect and non-defect cases. For practical classification, the Youden Index identifies the point on the ROC curve farthest from the chance diagonal, thereby maximizing the balance between sensitivity and specificity [34]. The resulting optimal threshold of $|A_r|$ was 3.858 mT, at which the true positive rate (TPR) reached 0.98, ensuring reliable defect detection while minimizing false alarms. As both threshold selection and evaluation were performed on the same dataset, these results should be regarded as exploratory; independent datasets will be required in future work to verify the generalizability of the chosen threshold.

A comparison of axial localization results obtained from $\sum(\Delta B_z)$ and $\sum B_r$ over 25 experimental sets is presented in Fig. 23. The results indicate a correlation coefficient of 0.999986, with a mean absolute error (MAE) of 1.67 mm and a root-mean-square error (RMSE) of 2.44 mm. The kernel density estimation (KDE) curve provided a smoothed visualization of the error distribution, indicating that most localization errors are concentrated within 2 mm [35]. Within tolerance ranges of ± 2 mm and ± 5 mm, the localization accuracies reach 75.4% and 94.9%, respectively. The strong agreement between the two components confirms their mutual consistency and enhances the reliability of the overall axial localization performance.

4.3. Circumferential and radial localization results

With axial localization established, defect localization was further investigated along the circumferential and radial axes. As shown in Fig. 24, each circumferential profile of the processed ΔB_z signal corresponded to one site along the horizontal axis, sampled at an axial defect location. Across 25 datasets with 7 peaks per scan, the horizontal axis therefore included 175 profiles (25 × 7) ordered by defect number within each dataset. The vertical axis listed all circumferential channels, each representing the processed ΔB_z values extracted at the corresponding axial peak positions. The bright regions indicated the circumferential areas associated with the defects, consistent with the peak-based circumferential localization method.

For radial localization, a multiclass ROC analysis based on the APV-FWHM feature was conducted on 25 experimental sets to evaluate the feasibility of depth discrimination. Specifically, the One-vs-Rest (OvR) strategy was employed, where each defect layer was sequentially regarded as the positive class and the remaining layers were merged as the negative class. The ROC curves of individual layers were **shown** in Fig. 25 (a). The macro-averaged AUC **reached** 0.921, indicating balanced discriminative performance across layers, while the micro-averaged AUC **was** 0.945, indicating strong overall separability. These results confirmed that the APV-FWHM feature offers strong statistical separability across different defect depths.

On this basis, the maximum a posteriori (MAP) decision rule was employed for multiclass discrimination [36]. Let the APV-FWHM feature of sample i be denoted as F_i. For the Gaussian statistical model corresponding to the j-th defect layer, the discrimination score is defined as:

$$S_{i,j} = \log p\left(F_i \mathrm{m}_j, \mathrm{s}_j\right) + \log \alpha_j \tag{29}$$

Here, m_j and s_j denote the mean and standard deviation of layer j, and α_j represents the prior probability. The predicted defect layer index of sample i is then determined by:

$$\widehat{\ell}_i = \arg\max_{j\in\{1,\ldots,7\}} S_{i,j} \tag{30}$$

that is, the defect layer with the maximum posterior score is selected as the final prediction. This guarantees unique classification of each sample and **enables statistical evaluation of performance using a confusion matrix**. The confusion matrix in Fig. 25 (b) shows that the strict layer

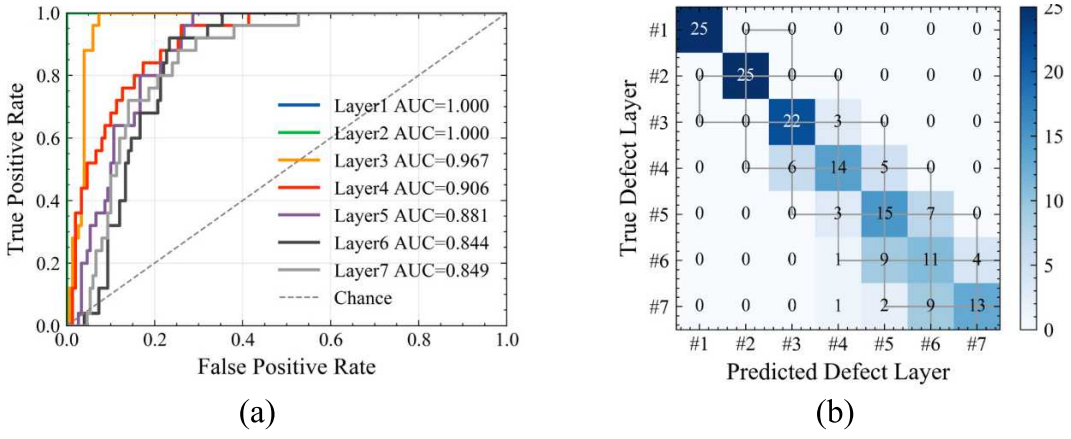

Fig. 25. Multiclass analysis of the APV-FWHM feature: (a) ROC curves of individual defect layers using the OvR strategy, showing strong separability across depths; (b) Confusion matrix of defect layer classification results obtained by the MAP decision rule.

classification accuracy **was** 71.4%. Allowing a tolerance of ±1 layer **increased** the accuracy to 97.7%.

For practical implementation, a standard set of APV-FWHM parameters can be established through pre-deployment calibration on a reference cable with certified defects.

5. Conclusion

This study proposes a defect localization method for bridge cables based on multi-component MFL testing, which employs spatial-domain summation preprocessing in the circumferential direction to enhance weak responses. The signal cross-validation is used for axial localization, and the APV-FWHM feature is adopted for depth localization, while peak-based circumferential localization is used to identify defect regions.

To validate the feasibility of this method, an experimental platform with triaxial Hall-sensor array was established, enabling synchronous acquisition of multi-component MFL signals. Experimental validation on a PECS7–127 cable indicated that all broken wires were successfully detected (175/175, 95% CI: 97.9–100%) at depths up to 42 mm. The signal cross-validation for axial localization accuracy reached 94.9% within a ± 5 mm tolerance. The circumferential regions of defects were effectively identified. The ROC analysis indicated that the APV-FWHM feature provides strong statistical separability across defect depths, while achieving a layer-wise depth estimation accuracy of 97.7% within a ± 1-layer tolerance. These results offer preliminary validation of the proposed method and indicate its effectiveness for defect testing and localization in bridge cables.

However, the present study was limited to the case of a single broken wire in bridge cables. Future research should aim to extend the methodology to encompass more complex defect scenarios, multi-wire defects and partial breaks, and enhance its engineering applicability.

CRediT authorship contribution statement

Huanze Liu: Writing – original draft, Validation, Software, Methodology, Investigation, Formal analysis, Conceptualization. **Lingsi Sun:** Writing – review & editing, Validation. **Runyu Wang:** Validation, Software, Data curation. **Yiqing Zou:** Writing – review & editing. **Xinjun Wu:** Writing – review & editing, Supervision, Resources, Project administration, Funding acquisition.

Declaration of competing interest

The authors declare that they have no known competing financial interests or personal relationships that could have appeared to influence the work reported in this paper.

Acknowledgments

This work was supported by the National Natural Science Foundation of China (Grant No. U21A20139).

Data availability

Data will be made available on request.

References

[1] Numerical investigation of cable breakage events on long-span cable-stayed bridges under stochastic traffic and wind, Eng. Struct. 105 (2015) 299–315, https://doi.org/10.1016/j.engstruct.2015.07.009.
[2] L. Sun, W. Zhang, H. Liu, R. Wang, S. Duan, L. Jiang, X. Wu, A quantitative evaluation method for broken wires in bridge cables using 3D spatially sampled magnetic flux leakage signals, NDT & E Int. 158 (2026) 103560, https://doi.org/10.1016/j.ndteint.2025.103560.
[3] X. Kong, Z. Liu, H. Liu, J. Hu, L. Deng, Recent advances on inspection, monitoring, and assessment of bridge cables, Autom. Constr. 168 (2024) 105767, https://doi.org/10.1016/j.autcon.2024.105767.
[4] B. Feng, J. Wu, H. Tu, J. Tang, Y. Kang, A review of magnetic flux leakage nondestructive testing, Materials 15 (2022) 7362, https://doi.org/10.3390/ma15207362.
[5] R. Christen, A. Bergamini, M. Motavalli, Three-dimensional localization of defects in stay cables using magnetic flux leakage methods, J. Nondestruct. Eval. 22 (2003) 93–101, https://doi.org/10.1023/B:JONE.0000010736.74285.b6.
[6] J. Xu, X. Wu, C. Cheng, A. Ben, A magnetic flux leakage and magnetostrictive guided wave hybrid transducer for detecting bridge cables, Sens 12 (2012) 518–533, https://doi.org/10.3390/s120100518.
[7] A. Ben, X. Wu, J. Yuan, Z. Xu, Analysis of Magnetic Flux Leakage of Broken Wire of Parallel Wire Strands Based on 3D Finite Element, Nondestructive Testing 33 (2011) 10–14.
[8] L. Sun, J. Wang, Z. Tao, S. Duan, X. Wu, A sensor based on multilayer-arranged hall elements for MFL detection of broken wires in bridge cables, Sens. Actuators, A 391 (2025) 116668, https://doi.org/10.1016/j.sna.2025.116668.
[9] Y. Qu, J. Zhou, R. Liu, L. Liao, Q. Zhao, Research on the detection of the broken wire damage of a cable in the circumferential directions based on self-magnetic flux leakage, KSCE J. Civ. Eng. 25 (2021) 879–890, https://doi.org/10.1007/s12205-021-0334-0.
[10] H. Tabatabai, National Cooperative Highway Research Program (NCHRP), Inspection and maintenance of bridge stay cable systems: a synthesis of highway practice, Transp. Res. Board (2005), https://doi.org/10.17226/13689.
[11] R. Schlanbusch, E. Oland, E.R. Bechhoefer, Condition monitoring technologies for steel wire ropes – a review, Int. J. Progn. Health Manag. 8 (2017), https://doi.org/10.36001/ijphm.2017.v8i1.2527.
[12] H.R. Vanaei, A. Eslami, A. Egbewande, A review on pipeline corrosion, in-line inspection (ILI), and corrosion growth rate models, Int. J. Press. Vessel. Pip. 149 (2017) 43–54, https://doi.org/10.1016/j.ijpvp.2016.11.007.
[13] W. Gong, M.F. Akbar, G.N. Jawad, M.F.P. Mohamed, M.N.A. Wahab, Nondestructive testing technologies for rail inspection: a review, Coatings 12 (2022) 1790, https://doi.org/10.3390/coatings12111790.
[14] Q. Chen, J. Zhang, B. Li, Research on 3D MFL testing of wire rope based on empirical wavelet transform and SRCNN, J. Vibroeng. 24 (2022) 779–792, https://doi.org/10.21595/jve.2022.22267.
[15] X. Chen, M. Fu, J. Shao, X. Liu, A cascaded pipeline defect detection and size estimation method based on the YOLOv11 and physics-informed network using the MFL data, Pet. Sci. (2025), https://doi.org/10.1016/j.petsci.2025.08.013.
[16] W. Gong, T. Yang, L. Guo, Magnetic flux leakage detection method by the arrays consisted of three-dimensional hall sensor for rail top surface cracks, Ferroelectrics 597 (2022) 52–64, https://doi.org/10.1080/00150193.2022.2091999.
[17] L. Sun, Z. Tao, Q. Ouyang, X. Wu, Development of multi-channel magnetic flux leakage testing system for bridge cables, E-j. Nondestruct. Test. 29 (2024), https://doi.org/10.58286/29932.
[18] J. Xue, E. Hu, Y. Sun, A wire rope defect signal enhancement method based on spatial domain array sensors combined with multi-process adaptive signal processing, Struct. Health Monit. (2025), https://doi.org/10.1177/14759217251360644.
[19] W. Liu, L. Ren, G. Tian, A novel defect quantification method utilizing multi-sensor magnetic flux leakage signal fusion, Sensors 24 (2024) 6623, https://doi.org/10.3390/s24206623.
[20] J. Wu, H. Fang, X. Huang, H. Xia, Y. Kang, C. Tang, An online MFL sensing method for steel pipe based on the magnetic guiding effect, Sensors 17 (2017) 2911, https://doi.org/10.3390/s17122911.
[21] M.X. Zambrano Otero, A. Martinez-de-Guerenu, F. Arizti, Magnetic flux leakage measurement system to detect flaws in small diameter metallic wire ropes, in: E-Journal of Nondestructive Testing, Czech Republic, Prague, 2014. https://www.ndt.net/?id=16700.
[22] L. Sun, X. Wu, Q. Ouyang, J. Wang, A novel broken wire evaluation method for bridge cable magnetic flux leakage testing under lift-off uncertainty, J. Magn. Magn. Mater. 570 (2023) 170525, https://doi.org/10.1016/j.jmmm.2023.170525.
[23] S. Hao, P. Shi, S. Su, T. Liang, Evaluation of defect depth in ferromagnetic materials via magnetic flux leakage method with a double hall sensor, J. Magn. Magn. Mater. 555 (2022) 169341, https://doi.org/10.1016/j.jmmm.2022.169341.
[24] O. Rainio, J. Hällilä, J. Teuho, R. Klén, Methods for estimating full width at half maximum, SIViP 19 (2025) 289, https://doi.org/10.1007/s11760-025-03820-6.

[25] Z. Tao, L. Sun, X. Wu, Design of magnetic flux leakage detection magnetizer for broken wire in bridge cable, Instrument Technique and Sensor 2025 (2025) 28–33.
[26] Standardization Administration of China, Hot-extruded PE protection paralleled high strength wire cable for cable-stayed bridge, 2018.
[27] Post-Tensioning Institute Cable-Stayed Bridge Committee, Recommendations for stay-cable design, testing and installation, Post-Tensioning Institute, 2012.
[28] H. Waisman, A. Montoya, R. Betti, I.C. Noyan, Load transfer and recovery length in parallel wires of suspension bridge cables, J. Eng. Mech. 137 (2011) 227–237, https://doi.org/10.1061/(ASCE)EM.1943-7889.0000220.
[29] T. Zhang, X. Xie, X. Pan, Tensile mechanical behavior of parallel wire cables with wire breaks, J. Zhejiang Univ. (Eng. Sci.) 50 (2016) 841–847, https://doi.org/10.3785/j.issn.1008-973X.2016.05.005.
[30] Y. Yu, Z. Chen, H. Liu, Advanced approaches to calculate recovery length and force redistribution in semi-parallel wire cables with broken wires, Eng. Struct. 131 (2017) 44–56, https://doi.org/10.1016/j.engstruct.2016.10.017.
[31] L. Deng, Y. Deng, Study on multi-crack damage evolution and fatigue life of corroded steel wires inside in-service bridge suspenders, Appl. Sci. 14 (2024) 9596, https://doi.org/10.3390/app14209596.
[32] T. Fawcett, An introduction to ROC analysis, Pattern Recogn. Lett. 27 (2006) 861–874, https://doi.org/10.1016/j.patrec.2005.10.010.
[33] J. Huang, C.X. Ling, Using AUC and accuracy in evaluating learning algorithms, IEEE Trans. Knowl. Data Eng. 17 (2005) 299–310, https://doi.org/10.1109/TKDE.2005.50.
[34] W.J. Youden, Index for rating diagnostic tests, Cancer 3 (1950) 32–35, https://doi.org/10.1002/1097-0142(1950)3:1%253C32::AID-CNCR2820030106%253E3.0.CO;2-3.
[35] B.W. Silverman, Density estimation for statistics and data analysis, 1st ed., Routledge, New York, 2018 https://doi.org/10.1201/9781315140919.
[36] C.M. Bishop, Pattern recognition and machine learning, Springer Science, New York, USA, 2007.